Talanta 233 (2021) 122563

Contents lists available at ScienceDirect

Talanta

journal homepage: www.elsevier.com/locate/talanta

Persistent luminescence nanorods-based autofluorescence-free biosensor for prostate-specific antigen detection

Zipeng Yin, Ling Zhu, Zijian Lv, Meijin Li **, Dianping Tang *

Key Laboratory for Analytical Science of Food Safety and Biology (MOE & Fujian Province), Fujian Provincial Key Laboratory of Electrochemical Energy Storage Materials, State Key Laboratory of Photocatalysis on Energy and Environment, Department of Chemistry, Fuzhou University, Fuzhou, 350108, PR China

ARTICLE INFO

Keywords:
Hybridization chain reaction
Autofluorescence-free biosensor
Persistent luminescence nanorods
Detection
Prostate-specific antigen

ABSTRACT

Persistent luminescent nanoparticles (PLNPs) are a class of materials with excellent optical properties, which can continue to emit light for a long time after removing the excitation light source. This feature enables PLNPs to be used for development of biological detection modes without autofluorescence background. In this study, we prepared Zn_2GeO_4: Mn^{2+}, Pr^{3+} (ZGOMP) nanorods through a one-pot hydrothermal method. Using the pH-responsive luminescence behavior of ZGOMP, we developed an autofluorescence-free biosensor using ZGOMP as a probe and gluconic acid as a quencher to detect prostate-specific antigen (PSA). Hybridization chain reaction (HCR) and magnetic separation system were introduced in the design to achieve efficient signal amplification. Under the optimal conditions, the as-designed autofluorescence-free sensing platform showed high selectivity, and showed a good luminescence response to PSA within the linear range of 0.001–10 ng/mL at a detection limit of 0.64 pg/mL. The excellent analytical performance shows that the current strategy provides an effective platform for clinical sample analysis.

1. Introduction

As is well-known, tumor markers are a kind of special biomarkers that can indicate whether cancer exists or not, and they can intuitively reflect the real-time situation of tumors *via* their quantitative changes. Prostate-specific antigen (PSA), a biomarker secreted by prostatic epithelial cells, is present in prostate tissue and semen [1,2]. The level of PSA in patients with prostate cancer is significantly higher than that of normal people. Since PSA level is a clear indicator of prostate cancer and only exists in specific tissues and organs, it is currently the preferred marker for the diagnosis of prostate cancer [3,4]. However, the extremely low level of PSA in human serum (4.0 ng/mL is regarded as the threshold for clinical screening of prostate cancer) force people to develop accurate, ultra-sensitive, and specific PSA detection methods for early diagnosis and recurrence monitoring of prostate cancer [5,6].

Fluorescent biosensors are widely used for the early diagnosis of cancers and show excellent performance in the detection of tumor markers. Compared with enzyme-linked immunosorbent assay (ELISA) [7,8], surface plasmon resonance (SPR) [9], electrochemical assay [10,11], colorimetric assay [12,13], and photoelectrochemical assay [14,15], the fluorescent assay has the advantages of high sensitivity, strong stability, and simple operation in trace determination [16,17]. Therefore, the development of more stable and sensitive fluorescent probes to construct more effective fluorescent sensors is of great significance for the early diagnosis of cancers. At present, a variety of materials, including quantum dots [18,19], metal nanoclusters [20,21], organic fluorescent dyes [22], metal-organic frameworks (MOF) [23] and so on, have been widely developed as fluorescent probes to monitor low levels of tumor markers. However, fluorescent sensors based on these materials often require continuous illumination of an excitation light source to generate a signal. Therefore, they cannot meet the needs of people to eliminate the background signal of the biological matrix for improving the signal-to-noise ratio [24].

In practical applications, materials with excellent optical properties are urgently needed to construct sensors with better performance. Fortunately, persistent luminescent nanoparticles (PLNPs), which can emit persistently after turning off the excitation light source, bring hope to researchers [25]. Because of its excellent optical properties, the sensor based on PLNPs does not need external illumination during detection, thus eliminating the interference of autofluorescence generated by the

* Corresponding author.
** Corresponding author.
E-mail addresses: mjli@fzu.edu.cn (M. Li), dianping.tang@fzu.edu.cn (D. Tang).

https://doi.org/10.1016/j.talanta.2021.122563
Received 15 April 2021; Received in revised form 10 May 2021; Accepted 24 May 2021
Available online 27 May 2021

biological matrix during *in-situ* excitation in actual detection process [26]. Many autofluorescence-free sensors based on PLNPs have been developed for *in vivo* bioimaging and *in vitro* biodetection [27–30]. Wang and co-workers established an autofluorescence-free sensing system for the sensitive detection of lysozyme in serum based on hydrothermally synthesized Zn_2GeO_4: Mn^{2+} persistent luminescence nanorods [31]. The Yan's group reported an aptasensor based on functionalized $ZnGa_2O_4$:Cr^{3+} persistent luminescent nanoparticles for sensitive autofluorescence-free determination of kanamycin in food samples [32]. Despite many advances in this field, ongoing effort has been made to explore innovative strategies for sensitivity improvement through nucleic acid signal amplification methods.

Herein, ZGOMP nanorods with great afterglow properties were synthesized by a simple one-pot hydrothermal method. It has been confirmed that ZGOMP is easily decomposed under acidic conditions, which leads to a significant decrease in the persistent luminescence (PL) signal of ZGOMP as the pH decreases. To this end, an autofluorescence-free sensor system for monitoring PSA levels was constructed. The magnetic separation system and hybridization chain reaction (HCR) process were introduced in this design to achieve signal amplification for effective improvement of sensitivity (Scheme 1). During the detection process, the presence of the target PSA induced the separation of PSA aptamer and tDNA and then triggered the HCR process, which resulted in a large amount of glucose oxidase (GOD) loading on the magnetic beads. Gluconic acid, derived from GOD catalytic product, can decompose ZGOMP and accurately monitored spectrometry in PL signal at 533 nm, which was also proportional to the concentration of PSA. Under the optimal conditions, the developed autofluorescence-free sensing system shows a wide linear range and a low detection limit. Overall, this work provides a feasible strategy for the application of persistent luminescent nanomaterials in sensitive biosensors and demonstrates the amazing application potential of autofluorescence-free sensing systems.

2. Experimental section

2.1. Reagents and chemicals

Avidin-GOD conjugates (2.0 mg/mL by UV absorbance at 280 nm; lyophilized; Buffer: 0.15 M sodium chloride + 0.02 M potassium phosphate, pH 7.2) were obtained from Rockland Immunochemicals Inc. (Limerick, Ireland). *N*-hydro-xysuccinimide (NHS) and *N*-(3-dimethylaminopropyl)-*N*′-ethylcarbo-diimide hydrochloride (EDC) were purchased from Sigma-Aldrich (Saint Louis, MO 63103, USA). Ammonium hydroxide ($NH_3{\cdot}H_2O$, 25 wt %), Carboxylated magnet beads (MBs), $Pr(NO_3)_3{\cdot}6H_2O$ (99.9%), germanium oxide (GeO_2, 99.999%), Manganese nitrate solution ($Mn(NO_3)_2$, 50% in H_2O) and Zn $(NO_3)_2{\cdot}6H_2O$ (99.9%) were purchased from Aladdin (Shanghai, China). All other reagents were of analytical grade and used without any further purification. Ultrapure water obtained from a Millipore water purification system (18.25 MΩ cm, Milli-Q, Millipore) was used in all runs. All buffers including phosphate-buffered saline (PBS) solution were the products of Sangon-Biotech (Shanghai, China). All sequences of the oligonucleotides were designed referring to the previous works (Table S1) [33].

2.2. Preparation of ZGOMP nanorods

ZGOMP nanorods were prepared through a one-step hydrothermal method [31,34]. Briefly, 1.0463 g GeO_2 powdered solid was dissolved in 25 mL NaOH solution (2.0 M) to prepare Na_2GeO_3 solution. With vigorous stirring, 300 μL concentrated HNO_3, 1.98 mmol of $Zn(NO_3)_2$, 0.01 mmol $Pr(NO_3)_3$, 0.01 mmol $Mn(NO_3)_2$, and 10 mL H_2O were mixed. After dropwise addition of 1.1 mmol Na_2GeO_3, a certain amount of $NH_3{\cdot}H_2O$ (25 wt %) was rapidly added to the solution prepared above to adjust the pH to 8.5, and continue magnetic stirring for 1 h at room temperature. Subsequently, the resulting white suspension was poured into a Teflon reactor to heat treatment for 16 h at 220 °C. Finally, the synthesized ZGOMP product was collected by centrifugation and washed alternately with ethanol and water four times, and then dried at 60 °C.

2.3. Preparation of anchor DNA-Modified magnetic beads (aDNA-MB)

The carboxylated magnetic beads (MB) were conjugated with aminated aDNA strands through a carbodiimide couple reaction [35]. First, the carboxylated MB (150 μL, 1.0 mg/mL, aqueous suspension) was injected into the MES buffer (1200 μL, 0.1 M, pH 6.0) containing NHS (2.5 mg/mL) and EDC (2.5 mg/mL). To fully activate the carboxyl group on MB, the mixture prepared above was reacted at 37 °C for 15 min. Subsequently, aDNA (150 μL, 200 μM) was mixed into the resulting mixture and kept shaking for 12 h at 37 °C. Magnetic separation was used to collect the product, and unbound biomolecules were washed away with PBS (10 mM pH 7.4). Finally, the aDNA-MB conjugates were dispersed in PBS (1.5 mL, 0.01 M, pH 7.4) and kept refrigerated at 4 °C.

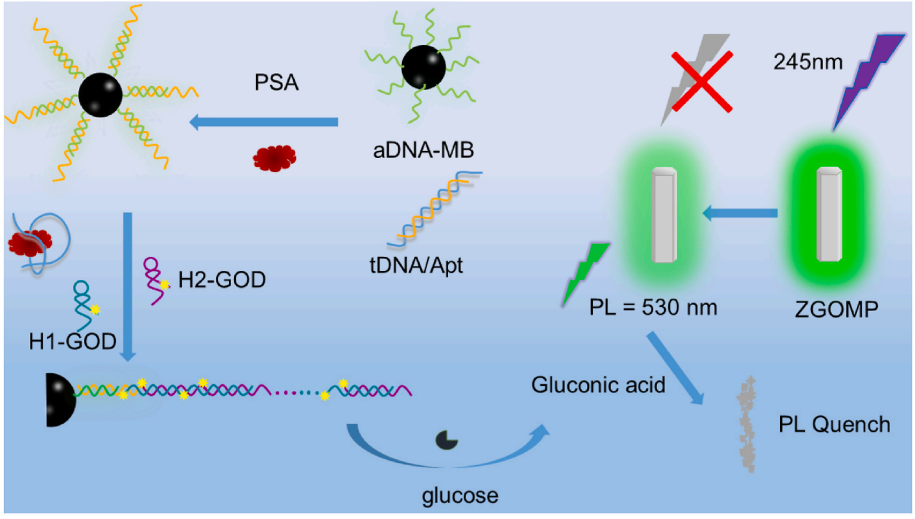

Scheme 1. Schematic Illustration of the autofluorescence-free sensing system for the detection of prostate-specific antigen (PSA). (H1: hairpin 1; H2: hairpin 2; aDNA: anchor DNA; tDNA: trigger DNA; Apt: PSA aptamer; MB: magnetic bead; GOD: glucose oxidase; PL: persistent luminescence).

2.4. Hybridization of trigger DNA with PSA aptamer (tDNA/Apt)

Briefly, PSA aptamer (10 μL, 100 μM) and tDNA (10 μL, 100 μM) were initially injected into PBS (180 μL, 0.01 M, pH 7.4). Thenceforth, the resultant mixture was annealed for 5 min at 95 °C and cooled naturally to room temperature. During this process, the added aptamer partially hybridized with tDNA to form an tDNA/Apt double-stranded structure with a concentration of 5.0 μM.

2.5. Procedure for the determination of PSA

PSA standard/sample with different concentrations (50 μL), tDNA/Apt (50 μL, 1.0 μM) and aDNA-MB conjugates (50 μL, 1.0 mg/mL) were initially mixed to react for 30 min at 25 °C. After magnetic separation, wash away unbound biomolecules with PBS (0.1 M, pH 7.4). Thereafter, the prepared mixture (50 μL) including GOD (1.0 U), Hairpin DNA1 (H1,10 μM), and Hairpin DNA2 (H2,10 μM) were added to the product obtained in the previous step. The mixture was incubated at room temperature for 40 min to fully perform the hybridization chain reaction (HCR) process between the two hairpin strands while allowing the avidin-glucose oxidase and the biotinylated DNA hairpin strands to bind as much as possible. After magnetic separation and washing, ZGOMP (100 μL, 0.75 mg/mL) and glucose (100 μL, 100 mM) were injected into the mixture, and reacted for 20 min. Finally, the PL intensity at 533 nm of the solution was measured for the determination of PSA on the fluorometer in the phosphorescence mode (excitation at 254 nm; the slit width for excitation and emission was set to 5.0 nm; the response time was set to 0.004 s).

3. Results and discussion

3.1. Characterization of ZGOMP nanorods

Mn^{2+}, Pr^{3+} doped Zn_2GeO_4 nanorods were synthesized *via* a one-pot hydrothermal strategy. In the process of hydrothermal synthesis, GeO_3^{2-} is hydrolyzed to GeO_4^{4-} [36]. When the concentrations of Zn^{2+} and GeO_4^{4-} reached a supersaturated state in the solution, Zn_2GeO_4 began to nucleate through the following process.

$$2Zn^{2+} + GeO_3^{2-} + 2OH^- = Zn_2GeO_4 + H_2O$$

It has been proved that ZnO_4 and GeO_4 tetrahedra be connected by forming the metal-oxygen-metal bonds, so that Zn_2GeO_4 nuclei continue to grow [37]. It is well known that the (110) plane (horizontal to the c-axis) has higher energy stability than the (001) plane, which makes ZGOMP nanoparticles preferentially grow along the c-axis direction like other nanomaterials with galena structure and finally assume the morphology of nanorods or nanowires [31,36]. ZGOMP samples (Fig. 1A) synthesized by the hydrothermal strategy showed uniformly distributed with clean surfaced rod-like structure as expected. The length and diameter of the ZGOMP nanorods were about 70–90 nm and 27–32 nm, respectively.

The XRD patterns (Fig. 1C) of the ZGOMP nanorods approximately in keeping with the standard pattern of Zn_2GeO_4 with the phenacite type structure (JCPDS No-110,687), which implied ZGOMP nanorods well maintained the rhombohedral phase structure. However, it was worth noting that the highest diffraction peaks of ZGOMP nanorods at 30.78° and 33.26° showed a blue shift compared with the standard pattern of Zn_2GeO_4, which indicated that the crystal lattice had slightly expanded (Fig. S1) [34]. X-ray photoelectron spectroscopy (XPS) of the resultant ZGOMP are shown in Fig. 1D. A double peak at 1021.4 eV and 1044.6 eV corresponded to the Zn^{2+}-2p level of $2p_{3/2}$ and $2p_{1/2}$, respectively, indicating that the chemical state of Zn^{2+} in ZGOMP. The characteristic peaks of Ge3d and O1s were observed at 32.0 eV and 530.8 eV, respectively, suggesting the existence of Ge^{4+} and O^{2-} in ZGOMP. Similarly, the peaks with binding energies at 933.6 eV and 929.8eV in the Pr XPS spectra were assigned to the peaks of Pr $3d_{5/2}$ and satellite peak, respectively, indicating that the chemical state of Pr is present as Pr^{3+} in ZGOMP (Fig. 1E) [38,39]. The binding energies of Mn $2P_{1/2}$ and Mn $2P_{3/2}$ are 655.3 and 640.9 eV, which can be attributed to the Mn^{2+} state existing in the composites (Fig. 1F). It must be noted that Mn^{2+}, Pr^{3+} and Zn^{2+} had similar valence and ionic radius, so they tended to substitute for Zn^{2+} in Zn_2GeO_4 crystal [40]. However, because the ionic radius of Pr^{3+} was larger than that of Zn^{2+} and the valence state was different, the substitution of Pr^{3+} for Zn^{2+} led to cation distortion and new defects. Meanwhile, this also explained the reason for the expansion of the Zn_2GeO_4 crystal lattice after the doping of Mn^{2+} and Pr^{3+} mentioned above. When two Zn^{2+} ions were replaced by two Pr^{3+} ions, in order to maintained charge balance, a vacancy defect with two negative charges (V''_{Zn}) and two positive defects of $Pr^{\cdot}_{Zn}$ were generated. Additionally, the aggregation of Pr^{3+} ions may change the depth of traps formed from the lattice defects, which is conducive to the generation of afterglow [41].

Fig. 1B shows the emission (Em) and excitation (Ex) spectra of ZGOMP, and the excitation band of ZGOMP can be clearly observed in the range of 215 nm–280 nm. Under the irradiation of 254 nm (the best excitation wavelength) excitation light, the symmetrical emission peak of ZGOMP appeared at about 533 nm. The persistent luminescence decay curve of ZGOMP showed that it still had a strong persistent luminescence after ceasing UV irradiation for 5 min, and the persistent luminescence of ZGOMP could still be observed by naked eyes even after stopping excitation for 0.5 h (Fig. S2). The green luminescence demonstrated that Mn^{2+} is tetrahedrally coordinated number of 4 rather than octahedrally coordinated number of 6 in the crystal lattice because the octahedral coordination will produce the red luminescence of Mn^{2+} [42,43]. For Pr^{3+}, previous studies [34,41] have pointed out that it only plays the role of trap center by forming positive defects ($Pr^{\cdot}_{Zn}$), not as the luminescent center. The mechanism for the persistent luminescence of ZGOMP is explained as follows (Fig. S3). On the one hand, the positively charged oxygen vacancy (V_O) and zinc interstitial ($Zn^{\cdot}_i$) form electron traps, and on the other hand, negatively charged germanium vacancy (V_{Ge}) and zinc vacancy (V''_{Zn}) form trap holes. When irradiated with ultraviolet light, energy was directly transferred from the excited electrons and holes through the crystal lattice to the luminescent center (Mn^{2+}), which immediately resulted in $^4T_1 \rightarrow {}^6A_1$ green emission of Mn^{2+} [41]. However, some of the excited electrons trapped by the oxygen vacancies do not immediately return to the ground state, but transfer to Pr^{3+} to form Pr^{2+} or $Pr^{3+} + e^-$ in the clusters. After ceasing the irradiation of UV light, with thermal stimulus, the electrons captured by Pr^{3+} are transferred to the luminescent center to combine with the opposite charges, thus realizing a characteristic persistent luminescence of Mn^{2+}.

3.2. Characteristics of HCR-based autofluorescence-free sensing system

To realize the high sensitivity detection of PSA, besides the synthesis of ZGOMP, some other issues about the construction of autofluorescence-free sensing detection system based on HCR deserve to be seriously studied, *e.g.*, (i) whether the PL signal of ZGOMP could produce different responses under different acidic conditions; (ii) whether tDNA could successfully trigger the HCR process and generate long duplexes as carriers for GOD landing; (iii) whether the products of the biological reaction triggered by the target (PSA) could effectively change the PL signal of ZGOMP.

To clarify these issues, the sustained luminescence spectra (Fig. 2D) of ZGOMP at different pH were first collected. It can be observed that the aqueous solution of ZGOMP at pH 7.0 was a milky white color, and after mixing with HAc-NaAc buffer solution of different pH, the solution gradually became transparent with the decrease of pH. Meanwhile, the green emission of ZGOMP under UV light gradually weakened and even completely disappeared. The morphological changes of ZGOMP at different pHs were observed by TEM (Fig. 2A–C). It can be seen that with the decrease of pH, ZGOMP occurred obvious decomposition,

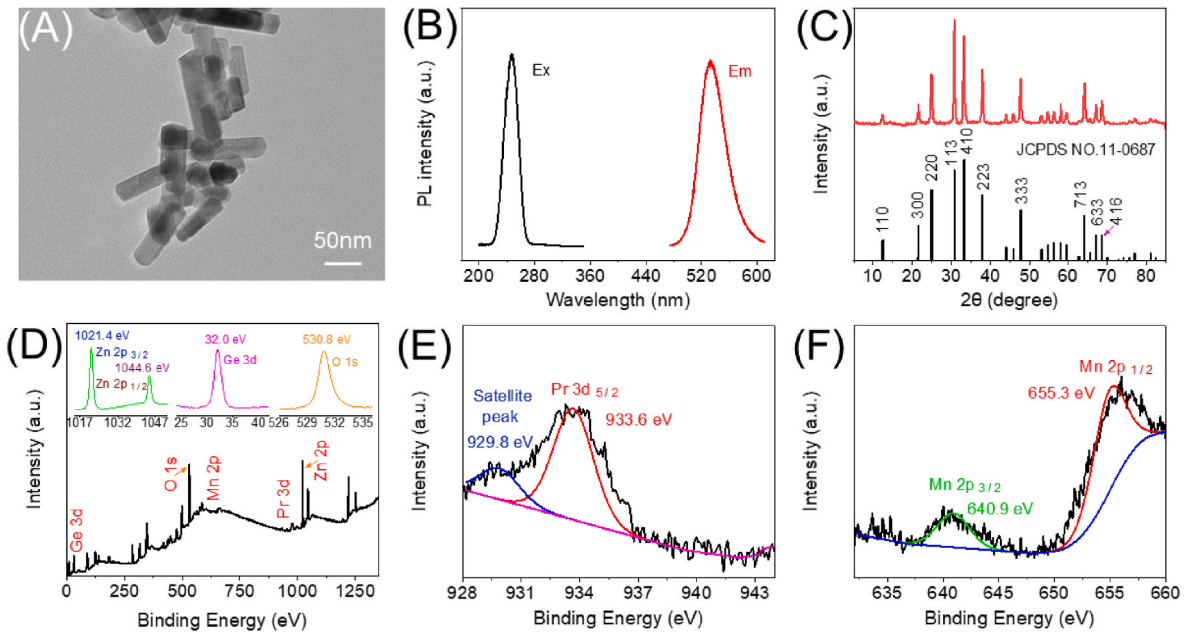

Fig. 1. (A) Transmission electron microscopy (TEM) image of ZGOMP; (B) Excitation (Ex) (phosphorescence mode at 533 nm) and emission (Em) (phosphorescence mode, excitation at 254 nm) spectra of ZGOMP; (C) Powder XRD patterns of ZGOMP; (D) XPS survey spectra of ZGOMP (inset, high-resolution XPS spectra of Zn 2p, Ge 3d and O1s), (E) Pr 3d, and (F) Mn 2p.

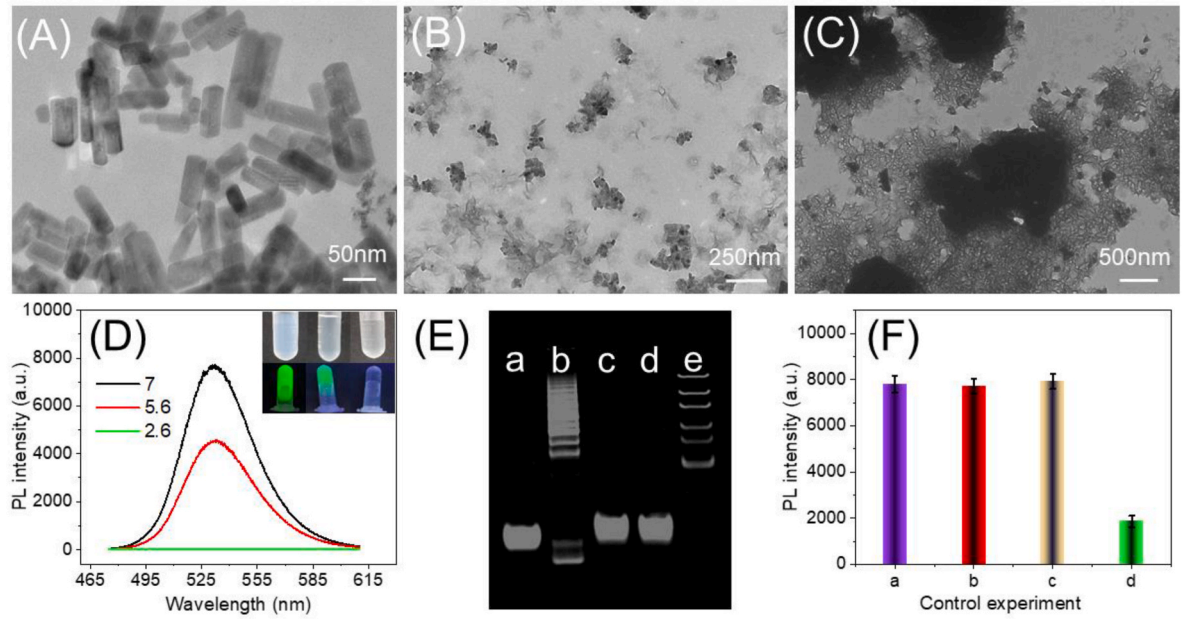

Fig. 2. (A–C) TEM images of ZGOMP at (A) pH 7.0, (B) pH 5.6 and (C) pH 2.6; (D) PL intensity of ZGOMP at 533 nm against pH in the acetic acid-sodium acetate buffer solution. Inset are photographs of ZGOMP solutions at pH 7.0, pH 5.6 and pH 2.6 under natural light and 254 nm UV lamp; (E) Gel electrophoresis (lane a: H1 + H2, lane b: H1 + H2 + tDNA, lane c: H1, lane d: H2, lane e: DNA marker); (F)PL intensity of (b) aDNA-MB + tDNA/Apt + GOD-H1/H2-GOD, (c) aDNA-MB + tDNA/Apt + GOD-H1/H2-GOD + glucose, (d) aDNA-MB + tDNA/Apt + GOD-H1/H2-GOD + glucose + PSA (note: Curve '*a*' gives the PL intensity of ZGOMP) (0.5 ng/mL PSA used in this case).

accompanied by the occurrence of agglomeration phenomenon. It is well known that strong acids can react with weak acid salts to generate the corresponding strong acid salts and weak acids. Therefore, the above phenomenon could be explained that the acidity of acetic acid was stronger than that of H_4GeO_4, and GeO^{4-} could be replaced from Zn_2GeO_4 to generate H_4GeO_4 and Zn^{2+}. Finally, acetic acid degraded ZGOMP and quenched its luminescence. Similarly, it could be speculated that gluconic acid, which was more acidic than acetic acid, could also quench the PL signal of ZGOMP in this way.

To verify that the presence of H1 and H2, tDNA can indeed induce the HCR process to form a long nicked DNA double-helix polymer, we employed gel electrophoresis. As shown in Fig. 2E, only one bright band could be found in the presence of either H1 or H2 (lane '*c*' and '*d*'). Lane '*a*' showed that only when H1 and H2 were mixed, the band did not change significantly, indicating that HCR process did not occur. However, when H1, H2 and tDNA were mixed, the bands appear as ladder-like extensions. These results demonstrated that the HCR process could be triggered only by the induction of tDNA to form nicked double-

helical DNA polymers of different lengths (Lane '*b*').

Although the above results have fully explained the signal transduction and amplification mechanism, the reliability of the detection process of the HCR-based sensor system still needs to be further verified. Therefore, we compared the PL signal under different conditions through several control experiments(Fig. 2F). Obviously, when ZGOMP, aDNA-MB, tDNA/Apt and GOD-H1/H2-GOD were present in the assay system, but glucose and PSA were absent (curve '*b*' and '*c*'), the PL signal of the system was almost identical to that of the blank group (curve '*a*') in which ZGMP was present alone. However, once all the necessary substances were present in the detection system, the PL signal was greatly reduced (curve '*d*' versus curve '*a*'). The results showed that the design of the detection process was reasonable, and the enzymatically produced gluconic acid could indeed degrade ZGOMP and quench its PL signal as expected.

3.3. Optimization of experimental conditions

As mentioned above, as the key steps of signal transduction and signal amplification, the catalytic process of glucose by GOD and the HCR process determined the performance of the autofluorescence-free sensing platform. To fully exploit the maximum potential of the detection platform, the optimal reaction time of the above two steps was explored. First, the binding reaction of biotinylated single-stranded DNA to avidin-GOD was performed simultaneously with the HCR process, different reaction times were set and the PL signals of the system were recorded (Fig. 3A). It was observed that the PL signal of the system was almost completely quenched after 40 min, indicating that the HCR process and the GOD attachment process had been fully completed within 40 min. To save time, 40 min was considered as the best reaction time for HCR process because the PL signal was not significantly weakened after 40 min. Besides, the optimal reaction time for the process of GOD catalyzing glucose was investigated in the same manner (Fig. 3B). The results showed that the PL signal of ZGOMP could be almost completely quenched by the biological reaction products in the system within 30 min. Therefore, 30 min was employed as the best catalysis time for GOD towards the substrate glucose.

3.4. Analytical performance of autofluorescence-free sensing system

Under optimal conditions, the analytical performance of the autofluorescence-free sensing system based on ZGOMP and HCR process was studied with different concentrations of PSA standard samples. It can be seen from Fig. 4A that the PL signal of the system decreases with increasing PSA concentration. The decreased PL intensity was linearly related to the logarithm of the concentration of PSA in the range of 0.001–10 ng/mL (Fig. 4B). The linear regression equation was $\Delta F = 1725.1 \times \log C_{[PSA]} + 452.8$ ($R^2 = 0.9941$, $n = 9$). The detection limit was approximately 0.64 pg/mL at the signal-to-noise ratio of 3σ (where σ is the standard deviation of a blank sample, $n = 11$, *i.e.*, IUPAC recommended method,1978). Impressively, the LOD value of this strategy was lower than the clinical diagnostic standard value of prostate cancer, which could fully meet the needs of PSA detection.

The ability to accurately monitor PSA in complex matrices was required for ZGOMP and HCR process-based sensing systems autofluorescence-free to be used in the clinical diagnosis of prostate cancer. Several biomarkers, including immunoglobulin G (IgG), carcinoembryonic antigen (CEA), cancer antigen 15–3 (CA 15–3) and alpha-fetoprotein (AFP) were used to challenge the accuracy of autofluorescence-free sensing systems for monitoring PSA concentrations (Fig. 4C). The autofluorescence-free sensing system had essentially no response to IgG, CEA, CA 15–3 and AFP compared to the significant decreased in PL signal in the presence of PSA. Moreover, when PSA coexisted with interfering biomarkers, the PL signal of the system did not change significantly compared with that of PSA alone. Also, a comparison of our strategy with several methods for PSA detection developed by other researchers is listed in Table S2. Compared with other PSA detection methods, this autofluorescence-free sensing platform based on ZGOMP and HCR process achieved more sensitive PSA detection. All in all, the above experimental results showed that the designed autofluorescence-free sensing system based on ZGOMP and HCR process has reliable selectivity.

3.5. Preliminary application in real samples

To further evaluate the potential of our design for practical sample testing, seven human serum samples from local Fujian Provincial Hospital were tested with the self-developed autofluorescence-free sensor system and commercial enzyme-linked immunosorbent assay (ELISA) kit, respectively. It should be noted that all human serum high concentration samples were well shaken and diluted with PBS buffer before being measured by these two methods. At the end of the test procedure, the PSA levels were calculated from the linear regression equation in Fig. 4B. The results are listed in Table 1 and are compared with the results of ELISA. In order to intuitively and correctly judged the reliability of the two detection methods, the *t*-test statistical analysis method was used to obtain the t_{exp} values between the two detection methods. It could be found that all t_{exp} values were lower than t_{crit} ($t_{crit\ [4,\ 0.05]} = 2.78$) [44,45], so it could be judged that there was no significant difference between the two methods at the 5% significance level. In other words, both methods have reliable accuracy, indicating that the autofluorescence-free sensing system based on ZGOMP and HCR processes is very promising for the detection of PSA in complex matrices.

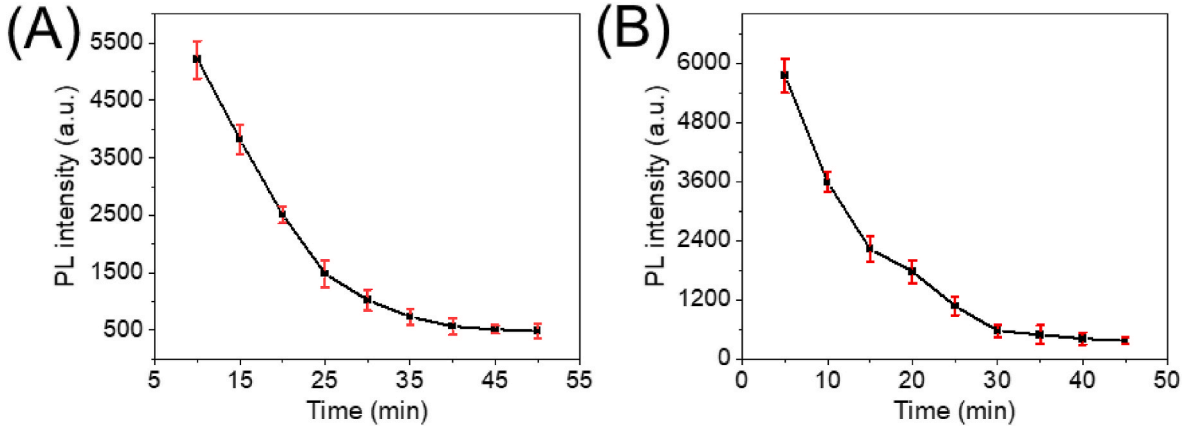

Fig. 3. (A) HCR time and (B) catalysis time on PL intensity responses of the autofluorescence-free sensing system (10 ng/mL PSA used as an example).

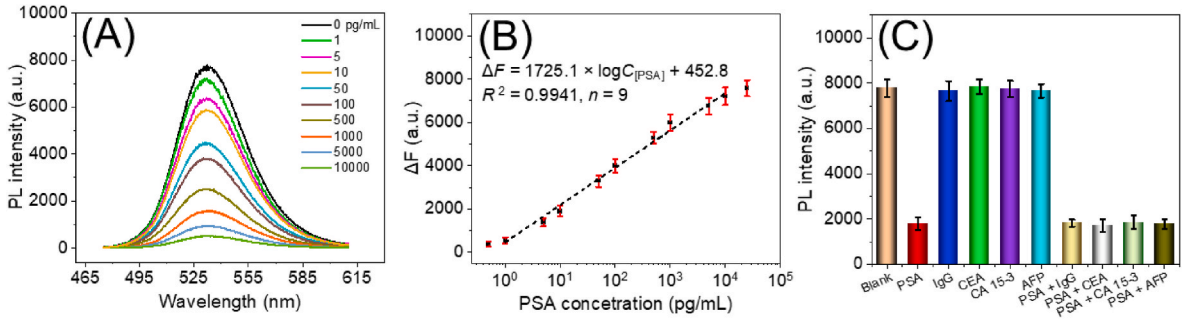

Fig. 4. (A)PL intensity of autofluorescence-free sensing system towards PSA standards with different concentrations; (B) calibration plots; (C) selectivity of autofluorescence-free sensing system against PSA (0.5 ng/mL), IgG (5.0 ng/mL), CEA (5.0 ng/mL), CA 15–3 (5.0 ng/mL) and AFP (5.0 ng/mL).

Table 1
Comparison of the results obtained by ZGOMP-based autofluorescence-free sensing system and commercial human PSA ELISA kit.

Sample no.	Method; concentration (mean ± SD, ng/mL, $n = 3$)		t_{exp}
	Autofluorescence-free sensing assay	PSA ELISA kit	
1	8.95 ± 0.59	9.63 ± 0.53	1.49
2	0.97 ± 0.06	0.93 ± 0.06	0.71
3	1.96 ± 0.15	2.04 ± 0.17	0.60
4	5.66 ± 0.34	5.75 ± 0.33	0.33
5	9.59 ± 0.46	10.59 ± 0.54	2.47
6	1.20 ± 0.03	1.23 ± 0.03	1.08
7	4.87 ± 0.31	4.77 ± 0.31	0.37

4. Conclusions

In summary, ZGOMP nanoparticles with great persistent luminescence properties have been successfully prepared and applied to construct a sensing platform without autofluorescence for PSA detection. Under acidic conditions, the PL signal of ZGOMP decreases with the decrease of pH, showing a sensitive acid response, which constitutes an important basis for the signal conversion of the concentration of PSA. Besides, the HCR process triggered by the target PSA caused a large amount of GOD to be loaded on the magnetic bead surface. The PL signal of ZGOMP was quenched by gluconic acid generated by enzyme catalysis in the detection system, which enabled the expected signal amplification effect to be achieved. The autofluorescence-free sensing system based on the ZGOMP and HCR process exhibit the advantages of wide linear range, low detection limit, high accuracy and good selectivity, which show that it has good application prospect in PSA detection with high efficiency, high sensitivity and low cost.

Credit author statement

Zipeng Yin: Conceptualization, Methodology, Visualization, Writing – original draft; **Ling Zhu**: Visualization, Conceptualization, Investigation, Writing – original draft; **Zijian Lv**: Methodology, Visualization, Investigation; **Meijin Li**: Project administration, Writing – review & editing; **Dianping Tang**: Supervision, Funding acquisition, Project administration, Writing – review & editing.

Declaration of competing interest

The authors declare that they have no known competing financial interests or personal relationships that could have appeared to influence the work reported in this paper.

Acknowledgments

The authors acknowledge financial support from the National Natural Science Foundation of China (grant nos.: 21874022 & 21675029).

Appendix A. Supplementary data

Supplementary data to this article can be found online at https://doi.org/10.1016/j.talanta.2021.122563.

References

[1] Q. Hu, S. Gan, Y. Bao, Y. Zhang, D. Han, L. Niu, Electrochemically controlled ATRP for cleavage-based electrochemical detection of the prostate-specific antigen at femtomolar level concentrations, Anal. Chem. 92 (2020) 15982–15988.
[2] K. Zhang, S. Lv, Z. Lin, D. Tang, CdS:Mn quantum dot-functionalized g-C_3N_4 nanohybrids as signal-generation tags for photoelectrochemical immunoassay of prostate specific antigen coupling DNAzyme concatamer with enzymatic biocatalytic preciption, Biosens. Bioelectron. 95 (2017) 34–40.
[3] O. Yavas, M. Svedendahl, P. Dobosz, V. Sanz, R. Quidant, On-a-chip biosensing based on all-dielectric nanoresonators, Nano Lett. 17 (2017) 4421–4426.
[4] Y. Wei, D. Wang, Y. Zhang, J. Sui, Z. Xu, Multicolor and photothermal dual-readout biosensor for visual detection of prostate specific antigen, Biosens. Bioelectron. 140 (2019) 111345.
[5] L. Tang, S. Li, L. Xu, W. Ma, H. Kuang, L. Wang, C. Xu, Chirality-based Au@Ag nanorod dimers sensor for ultrasensitive PSA detection, ACS Appl. Mater. Interfaces 7 (2015) 12708–12712.
[6] G. Ertürk, H. Özen, M. Tümer, B. Mattiasson, A. Denizli, Microcontact imprinting based surface plasmon resonance (SPR) biosensor for real-time and ultrasensitive detection of prostate specific antigen (PSA) from clinical samples, Sens. Actuators, B 224 (2016) 823–832.
[7] G. Gutierrez-Zuniga, J. Hernandez-Lopez, Sensitivity improvement of a sandwich-type ELISA immunosensor for the detection of different prostate-specific antigen isoforms in human serum using electrochemical impedance spectroscopy and an ordered and hierarchically organized interfacial supramolecular architecture, Anal. Chim. Acta 902 (2016) 97–106.
[8] Y. Gao, Y. Zhou, R. Chandrawati, Metal and metal oxide nanoparticles to enhance the performance of enzyme-linked immunosorbent assay (ELISA), ACS Appl. Nano Mater. 3 (2019) 1–21.
[9] J. Masson, Surface plasmon resonance clinical biosensors for medical diagnostics, ACS Sens. 2 (2017) 16–30.
[10] D. Sadighbayan, K. Sadighbayan, M. Tohid-kia, A. Khosroushahi, M. Hasanzadeh, Development of electrochemical biosensors for tumor marker determination towards cancer diagnosis: recent progress, Trends Anal. Chem. 118 (2019) 73–88.
[11] R. Zeng, L. Su, Z. Luo, L. Zhang, M. Lu, D. Tang, Ultrasensitive and label-free electrochemical aptasensor of kanamycin coupling with hybridization chain reaction and strand-displacement amplification, Anal. Chim. Acta 1038 (2018) 21–28.
[12] Z. Gao, S. Shao, W. Gao, D. Tang, D. Tang, S. Zou, M. Kim, X. Xia, Morphology-invariant metallic nanoparticles with tunable plasmonic properties, ACS Nano 15 (2021) 2428–2438.
[13] L. Tang, J. Li, Plasmon-based colorimetric nanosensors for ultrasensitive molecular diagnostics, ACS Sens. 2 (2017) 857–875.
[14] J. Shu, D. Tang, Recent advances in photoelectrochemical sensing: from engineered photoactive materials to sensing devices and detection modes, Anal. Chem. 92 (2020) 363–377.
[15] F. Li, Y. Zhou, H. Yin, S. Ai, Recent advances on signal amplification strategies in photoelectrochemical sensing of microRNAs, Biosens. Bioelectron. 166 (2020) 112476.
[16] P. Roidos, S. Sungalee, S. Benfatto, O. Sercin, A. Stutz, A. Abdollahi, J. Mauer, F. Zenke, J. Korbel, B. Mardin, A scalable CRISPR/Cas9-based fluorescent reporter assay to study DNA double-strand break repair choice, Nat. Commun. 11 (2020) 4077.
[17] D. Wu, A. Sedgwick, T. Gunnlaugsson, E. Akkaya, J. Yoon, T. James, Fluorescent chemosensors: the past, present and future, Chem. Soc. Rev. 46 (2017) 7105–7123.
[18] M. Chern, P. Garden, R. Baer, J. Galagan, A. Dennis, Transcription factor based small-molecule sensing with a rapid cell phone enabled fluorescent bead assay, Angew. Chem. Int. Ed. 59 (2020) 21597–21602.

[19] L. Saa, V. Pavlov, Enzymatic growth of quantum dots: applications to probe glucose oxidase and horseradish peroxidase and sense glucose, Small 8 (2012) 3449–3455.
[20] R. Liu, S. Duan, L. Bao, Z. Wu, J. Zhou, R. Yu, Photonic crystal enhanced gold-silver nanoclusters fluorescent sensor for Hg^{2+} ion, Anal. Chim. Acta 1114 (2020) 50–57.
[21] L. Zhang, E. Wang, Metal nanoclusters: new fluorescent probes for sensors and bioimaging, Nano Today 9 (2014) 132–157.
[22] Y. Poronik, K. Vygranenko, D. Gryko, D. Gryko, Rhodols - synthesis, photophysical properties and applications as fluorescent probes, Chem. Soc. Rev. 48 (2019) 5242–5265.
[23] S. Wu, H. Min, W. Shi, P. Cheng, Multicenter metal-organic framework-based ratiometric fluorescent sensors, Adv. Mater. 32 (2020), e1805871.
[24] X. Zhao, L. Chen, K. Zhao, Y. Liu, J. Liu, X. Yan, Autofluorescence-free chemo/biosensing in complex matrixes based on persistent luminescence nanoparticles, Trends Anal. Chem. 118 (2019) 65–72.
[25] L. Shi, J. Shao, X. Jing, W. Zheng, H. Liu, Y. Zhao, Autoluminescence-free dual tumor marker biosensing by persistent luminescence nanostructures, ACS Sustain. Chem. Eng. 8 (2019) 686–694.
[26] L. Shi, W. Zheng, H. Miao, H. Liu, X. Jing, Y. Zhao, Ratiometric persistent luminescence aptasensors for carcinoembryonic antigen detection, Mikrochim. Acta 187 (2020) 615.
[27] H. Zhao, G. Shu, J. Zhu, Y. Fu, Z. Gu, D. Yang, Persistent luminescent metal-organic frameworks with long-lasting near infrared emission for tumor site activated imaging and drug delivery, Biomaterials 217 (2019) 119332.
[28] N. Li, Y. Li, Y. Han, W. Pan, T. Zhang, B. Tang, A highly selective and instantaneous nanoprobe for detection and imaging of ascorbic acid in living cells and in vivo, Anal. Chem. 86 (2014) 3924–3930.
[29] Y. Zhao, F. Zheng, L. Shi, H. Liu, W. Ke, Autoluminescence-free prostate-specific antigen detection by persistent luminous nanorods and Au@Ag@SiO2 nanoparticles, ACS Appl. Mater. Interfaces 11 (2019) 40669–40676.
[30] H. Liu, F. Ren, X. Zhou, C. Ma, T. Wang, H. Zhang, Q. Sun, Z. Li, Ultra-sensitive detection and inhibition of the metastasis of breast cancer cells to adjacent lymph nodes and distant organs by using long-persistent luminescence nanoparticles, Anal. Chem. 91 (2019) 15064–15072.
[31] J. Wang, Q. Ma, W. Zheng, H. Liu, C. Yin, F. Wang, X. Chen, Q. Yuan, W. Tan, One-dimensional luminous nanorods featuring tunable persistent luminescence for autofluorescence-free biosensing, ACS Nano 11 (2017) 8185–8191.
[32] B. Wang, X. Zhao, L. Chen, C. Yang, X. Yan, Functionalized persistent luminescence nanoparticle-based aptasensor for autofluorescence-free determination of kanamycin in food samples, Anal. Chem. 93 (2021) 2589–2595.
[33] Q. Zhou, Y. Lin, K. Zhang, M. Li, D. Tang, Reduced graphene oxide/BiFeO3 nanohybrids-based signal-on photoelectrochemical sensing system for prostate-specific antigen detection coupling with magnetic microfluidic device, Biosens. Bioelectron. 101 (2018) 146–152.
[34] J. Li, X. Huang, X. Zhao, L. Chen, X. Yan, pH-responsive torpedo-like persistent luminescence nanoparticles for autofluorescence-free biosensing and high-level information encryption, Angew. Chem. Int. Ed. 60 (2021) 2398–2405.
[35] P. Zhang, F. Cheng, R. Zhou, J. Cao, J. Li, C. Burda, Q. Min, J. Zhu, DNA-hybrid-gated multifunctional mesoporous silica nanocarriers for dual-targeted and microRNA-responsive controlled drug delivery, Angew. Chem. Int. Ed. 53 (2014) 2371–2375.
[36] B. Srivastava, S. Gupta, Y. Li, Y. Mao, Bright persistent green emitting water-dispersible Zn2GeO4:Mn nanorods, Dalton Trans. 49 (2020) 7328–7340.
[37] S. Yan, L. Wan, Z. Li, Z. Zou, Facile temperature-controlled synthesis of hexagonal Zn2GeO4 nanorods with different aspect ratios toward improved photocatalytic activity for overall water splitting and photoreduction of CO_2, Chem. Commun. 47 (2011) 5632–5634.
[38] J. Kim, C. Na, C. Kwak, H. Li, J. Yoon, J. Kim, S. Jeong, J. Lee, Humidity-independent gas sensors using Pr-doped In_2O_3 macroporous spheres: role of cyclic Pr^{3+}/Pr^{4+} redox reactions in suppression of water-poisoning effect, ACS Appl. Mater. Interfaces 11 (2019) 25322–25329.
[39] M. Yagoub, H. Swart, E. Coetsee, Concentration quenching, surface and spectral analyses of $SrF_2:Pr^{3+}$ prepared by different synthesis techniques, Opt. Mater. 42 (2015) 204–209.
[40] X. Sun, Z. He, X. Gu, Persistent luminescence of $Zn_2GeO_4:Mn^{2+}/Pr^{3+}$ phosphors, J. Mater. Sci. Mater. Electron. 29 (2018) 17217–17221.
[41] M. Wan, Y. Wang, X. Wang, H. Zhao, Z. Hu, The properties of a novel green long afterglow phosphor $Zn_2GeO_4:Mn^{2+}$, Pr^{3+}, Opt. Mater. 36 (2014) 650–654.
[42] Q. Zhang, J. Wang, Synthesis and characterization of $Zn_2GeO_4:Mn^{2+}$ phosphor for field emission displays, Appl. Phys. A 108 (2012) 943–948.
[43] M. Shang, G. Li, D. Yang, X. Kang, C. Peng, Z. Cheng, J. Lin, Mg)2GeO4 Zn, Mn^{2+} submicrorods as promising green phosphors for field emission displays: hydrothermal synthesis and luminescence properties, Dalton Trans. 40 (2011) 9379–9387.
[44] Z. Yu, G. Cai, X. Liu, D. Tang, Pressure-based biosensor integrated with a flexible pressure sensor and an electrochromic device for visual detection, Anal. Chem. 93 (2021) 2916–2925.
[45] S. Lv, K. Zhang, L. Zhu, D. Tang, ZIF-8-assisted NaYF4:Yb,Tm@ZnO converter with exonuclease III-powered DNA walker for near-infrared light responsive biosensor, Anal. Chem. 92 (2020) 1470–1476.